Proceedings of the Thirty-sixth (2026) International Ocean and Polar Engineering Conference **www.isope.org**
Orlando, Florida, USA, May 31-June 5, 2026

ISBN 978-1-880653-72-2; ISSN 1098-6189

Study of the Influence of Hydrofoil AOA on Hydrodynamic Noise Sources

Chao Chen[1], Chen Niu[2], Yuan Zhuang[1], Decheng Wan[1]*

[1] Computational Marine Hydrodynamics Lab (CMHL), School of Ocean and Civil Engineering,
Shanghai Jiao Tong University, Shanghai, China
[2] Wuhan Second Ship Design and Research Institute, Wuhan, China
*Corresponding author

ABSTRACT

This study performed numerical simulations on the NACA 0012 hydrofoil with a Reynolds number of 360,000 using the Large Eddy Simulation (LES) method. The Farassat 1 A formula based on the Ffowcs Williams-Hawkings (FW-H) analogy was then used for flow noise calculations. Three different angles of attack (AOA) 0°, 4°, and 8° were investigated, and their effects on the spatial distribution of dipole and quadrupole acoustic sources were analyzed. The results indicate that the acoustic source distribution is relatively regular in laminar flow regions. As the AOA increases, the boundary separating the regular and irregular source distributions progressively shifts toward the leading edge of the hydrofoil. The findings of this study could provide reference for noise generation mechanisms and control technology.

KEY WORDS: NACA 0012; AOA; LES; Hydrodynamic noise; Sound source

INTRODUCTION

In recent years, driven by the increasing demand for the development of underwater equipment, growing attention has been paid to the study of flow-induced noise in underwater vehicles. Advanced acoustic technologies (Ohman et al., 2009) are of critical importance for improving the safety of underwater vehicles. As a typical class of underwater structures, hydrofoils have been extensively employed in fundamental research on the performance of underwater vehicles (Zhang et al., 2023), including cavitation suppression (Simanto et al., 2025) and noise control (Li et al., 2021), demonstrating significant scientific and research value.

With the development of computational fluid dynamics (CFD) techniques, numerical simulations have become an important approach for investigating flow and noise phenomena. Large eddy simulation (LES) is widely regarded as a relatively accurate method for simulating hydrodynamic and acoustic problems. Deng et al. (2024) investigated the cavitating flow around a NACA 0015 hydrofoil using three turbulence models, namely RANS, DES, and LES. Their results demonstrated that LES is capable of clearly reproducing vortex shedding patterns that are in good agreement with experimental observations.

In terms of noise prediction methodologies, the Ffowcs Williams–Hawkings (FW–H) acoustic analogy has been extensively applied to predict sound radiation generated by unsteady flows (Ma et al., 2024). Among its formulations, the Farassat 1 A equation exhibits superior numerical stability and prediction accuracy in time-domain calculations. Bulut et al. (2024) performed numerical simulations of flow-induced noise from cylinders with different shapes and aspect ratios using a permeable FW–H integration surface and compared the results with experimental data. The comparison showed that the maximum sound pressure level (SPL) discrepancy in the frequency domain did not exceed 2.4 dB, indicating the effectiveness of this approach.

With respect to the hydrodynamic noise of hydrofoils, Hu et al. (2022) investigated the effects of trailing-edge serrations with different lengths on the flow-induced noise reduction of a NACA 0012 hydrofoil. The results indicated that serrations of moderate length achieve the optimal noise reduction performance, with a maximum reduction in the overall sound pressure level (OASPL) of approximately 2.4 dB, suggesting that serration length has a significant influence on noise reduction effectiveness. Kim et al. (2016) and Chen et al. (2018) examined the effects of leading-edge modifications by introducing wavy leading edges to the hydrofoil, focusing on the influence of leading-edge protuberances with different sizes on flow-induced noise. Their studies revealed the existence of a phase interference effect among different protuberance geometries, which reduces pressure fluctuations on the hydrofoil surface and consequently decreases the sound source levels.

At present, research on hydrofoil flow-induced noise is predominantly focused on monitoring-point-based metrics such as variations in OASPL, spectral characteristics, and directivity. In contrast, relatively limited attention has been paid to the spatial distribution of surface acoustic sources. In particular, studies employing a controlled-variable approach to investigate the effects of a single parameter on surface sound source distribution remain relatively underexplored. Investigating the surface sound source distribution of the object could provide some insights into noise generation mechanisms, which in turn can offer a theoretical foundation for noise control technologies, such as hydrofoil shape optimization.

Based on the background mentioned above, this study combines LES with the FW-H acoustic analogy method to numerically investigate the flow and sound source characteristics of the NACA 0012 hydrofoil under different AOAs. The impact of the variation in AOA on the flow structure is discussed first, followed by an analysis of the distribution characteristics of dipole and quadrupole sound sources on the suction surface, pressure surface, and mid-span slice. The OASPL of the dipole and quadrupole terms at different azimuths is then analyzed. This analysis aims to reveal the mechanism by which the flow structure affects the sound source. The findings of this study could provide reference into the analysis of flow-induced noise mechanisms in underwater vehicles and serve as a basis for subsequent noise prediction and control research.

NUMERICAL METHOD

Governing Equation

This study employs the LES method, as referenced by Xie et al. (2025). The governing equations for incompressible viscous fluid are as follows:

$$\frac{\partial \overline{u_i}}{\partial x_i} = 0 \tag{1}$$

$$\frac{\partial \left(\overline{u_i}\right)}{\partial t} + \frac{\partial}{\partial x_j}\left(\rho \overline{u_i}\,\overline{u_j}\right) = -\frac{1}{\rho}\frac{\partial \overline{p}}{\partial x_i} + \nu \frac{\partial^2 u_i}{\partial x_j^2} - \frac{\partial \tau_{ij}}{\partial x_j} \tag{2}$$

where u represents the fluid velocity, the symbol $\bar{}$ represents the spatial filtering, p is the pressure, ν is the kinematic viscosity, $\tau_{ij} = \overline{u_i}\,\overline{u_j} - \overline{u_i u_j}$ is the sub-grid stress to describe the interactions between the large-scale eddies and small-scale eddies.

In LES, there are three main subgrid-scale models: the Smagorinsky subgrid-scale model, the dynamic Smagorinsky subgrid-scale model, and the wall-adapting local eddy-viscosity (WALE) subgrid-scale model, WALE takes both the shear stress tensor and the rotation tensor into account, the expression of subgrid viscosity of WALE is as follows:

$$\nu_t = \left(c_w\right)^2 \frac{\left(S_{ij}^d S_{ij}^d\right)^{\frac{3}{2}}}{\left(\overline{S}_{ij}\overline{S}_{ij}\right)^{\frac{5}{2}} + \left(S_{ij}^d S_{ij}^d\right)^{\frac{5}{4}}} \tag{3}$$

$$S_{ij}^d = \frac{1}{2}\left(\frac{\partial \overline{u}_i}{\partial x_k}\frac{\partial \overline{u}_k}{\partial x_j} + \frac{\partial \overline{u}_j}{\partial x_k}\frac{\partial \overline{u}_k}{\partial x_i}\right) - \frac{1}{3}\delta_{ij}\frac{\partial \overline{u}_k}{\partial x_k}\frac{\partial \overline{u}_k}{\partial x_k} \tag{4}$$

where C_w is the model coefficient, Δ is the grid filter width defined by c ell volume.

The FW-H acoustic analogy equation precisely reorganizes the continui ty and momentum equations into a form of the non-homogeneous wave equation, and its form is as follows:

$$\left(\frac{\partial^2}{\partial t^2} - c_0^2\frac{\partial^2}{\partial x_i^2}\right)\rho' = \frac{\partial}{\partial t}\left\{\left[\rho\left(v_i - u_i\right) + \rho_0 v_i\right]\delta\left(f\right)\frac{\partial f}{\partial x_i}\right\} - \frac{\partial}{\partial x_i}\left\{\left[\rho v_i\left(v_j - u_j\right) + P_{ij}\right]\delta\left(f\right)\frac{\partial f}{\partial x_j}\right\} + \frac{\partial^2}{\partial x_i \partial x_j}\left\{T_{ij}H\left(f\right)\right\} \tag{5}$$

Based on the FW-H equation, Farassat (2007) derived the Farassat 1 A formula, whose thickness term p_T', loading term p_L' are as follows:

$$4\pi p_T'\left(x,t\right) = \int_{f=0}\left[\frac{\rho_0 \dot{v}_n}{r(1-M_r)^2} + \frac{\rho_0 v_n \hat{r}_i \dot{M}_i}{r(1-M_r)^3}\right]_{ret} ds + \int_{f=0}\left[\frac{\rho_0 c v_n\left(M_r - M^2\right)}{r^2(1-M_r)^3}\right]_{ret} ds \tag{6}$$

$$4\pi p_L'\left(x,t\right) = \int_{f=0}\left[\frac{\dot{p}\cos\theta}{cr(1-M_r)^2} + \frac{\hat{r}_i \dot{M}_i\, p\cos\theta}{r(1-M_r)^3}\right]_{ret} ds + \int_{f=0}\left[\frac{p\left(\cos\theta - M_i n_i\right)}{r^2(1-M_r)^2} + \frac{p\cos\theta\left(M_r - M^2\right)}{r^2(1-M_r)^3}\right]_{ret} ds \tag{7}$$

As referenced by Xie et al. (2025), the quadrupole term p_Q' as follows:

$$4\pi p_Q'\left(x,t\right) = \frac{\partial^2}{\partial x_i \partial x_j}\int_V \left[\frac{T_{ij}}{r\left(1-M_r\right)}\right]_{ret} dV \tag{8}$$

$$T_{ij} = \rho u_i u_j + \delta_{ij}\left[(p - p_0) - c_0^2(\rho - \rho_0)\right] - \sigma_{ij} \tag{9}$$

where ρ_0 is the fluid density; $v_n = v \cdot n$, v is the velocity vector of the moving surface, and n is the unit normal vector pointing from the object surface towards the fluid. $\hat{r}$ is the unit vector from a point on the object surface to the observer. $M_i = v_i / c$, c is the speed of sound in fluid, and M is the Mach number, v_i is the component of the velocity vector on the moving object's surface. p is the physical surface pressure. $cos\theta = n \cdot \hat{r}$, $M_r = M \cdot \hat{r}$, the dot over a variable means time derivative. the subscript ''ret'' means that variables inside the square brackets are computed at the corresponding retarded time. u_i denotes the fluid velocity component in the i direction, $\delta(\cdot)$ is the Dirac delta function, σ_{ij} is the viscous stress tensor, T_{ij} denotes the Lighthill stress tensor.

GEOMETRY AND SETUP

Calculation Domain and Setup

In this paper, the NACA 0012 foil was used as the base model for calculation, The computational domain and boundary conditions are illustrated in Fig. 1. The inlet is about 4 C from the origin, and the outlet is about 10 C from the origin, the hydrofoil is located at the center of the semicircle. The chord length is C=0.1 m, and the spanwise length was set to 0.4 C. The corresponding Reynolds number is 360,000. The detailed geometric parameters and operating conditions are summarized in Table 1. The total physical simulation time was 1.5 s, with a time step size of 1×10^{-5} s, A second-order temporal discretization scheme was employed, and the pressure–velocity coupling was resolved using the SIMPLE implicit algorithm.

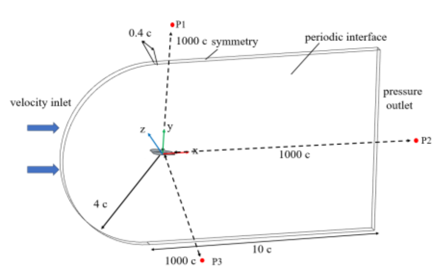

Fig. 1 Calculation domain and boundary conditions

To facilitate the analysis of the OASPL and spectral characteristics of the noise, three monitoring points were selected: directly above, directly behind, and directly to the lateral side of the airfoil, as shown by points P 1, P 2, and P 3 in the figure. Their coordinates are (0, 1000c, 0), (1000c, 0, 0), and (0, 0, -1000c), respectively.

Table 1. Calculation parameters of NACA 0012

NACA 0012	Value
Chord length(C)	0.1m
Angles of attack	0°, 4°, 8°
Reynolds number	3.6×10^5
U_0	3.6 m/s
Fluid density	1×10^3 kg/m^3

During the mesh generation process, a multi-level refinement strategy was adopted, as shown in

Fig. 2. A polyhedral mesh was employed for the numerical simulations, with prism layers generated adjacent to the hydrofoil surface. The growth rate of the prism layers was set to 1.1, and the thickness of the first prism layer is 0.003 mm to ensure that $y^+\leq1$.

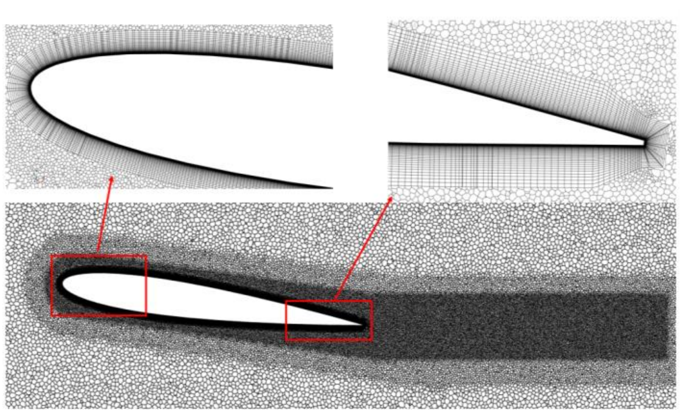

Fig. 2 Computational mesh

The distribution of y^+ values on the hydrofoil surface is shown in Fig. 3, where the maximum y^+ value is 0.747, satisfying the requirements for near-wall resolution in the present simulations.

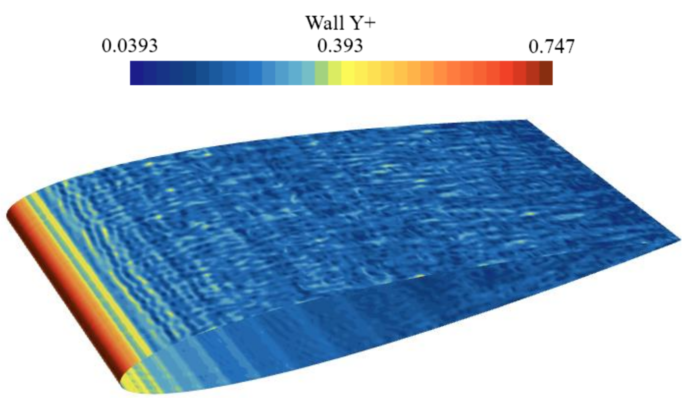

Fig. 3 The y^+ distribution on the hydrofoil surface

Numerical Validation

Sheldahl R E et al. (1981) conducted experimental investigations on airfoil performance under different Reynolds numbers and angles of attack. The lift coefficient is defined as:

$$C_l = \frac{F_l}{0.5\rho U_0^2 A} \tag{10}$$

The drag coefficient is defined as:

$$C_d = \frac{F_d}{0.5\rho U_0^2 A} \tag{11}$$

where F_l is the perpendicular lift force to the direction of the incoming flow, F_d is the resistance parallel to the incoming flow direction. A is the projected area of the NACA 0012 hydrofoil.

Table 2. Comparison of experimental and LES results for C_l

	Exp	LES	error (%)
0°	0	0.0010	
4°	0.4400	0.4434	0.77
8°	0.8542	0.8687	1.70

Table 3. Comparison of experimental and LES results for C_d

	Exp	LES	error (%)
0°	0.0079	0.0080	1.27
4°	0.0098	0.0096	-2.04
8°	0.0153	0.0150	-1.96

The numerical simulation values and experimental values of C_l and C_d at different AOA are compared in Table 2, Table 3. The LES values were taken as the average of the last 0.1 seconds, and the maximum relative error does not exceed 2.04%, indicating that the current numerical method has a certain level of accuracy. The time histories of the C_l and C_d over the final 0.1 s are shown in

, Fig. 5 and Fig. 6. Both coefficients exhibit smooth, periodic fluctuations around their mean values, indicating that the flow has reached a statistically steady state.

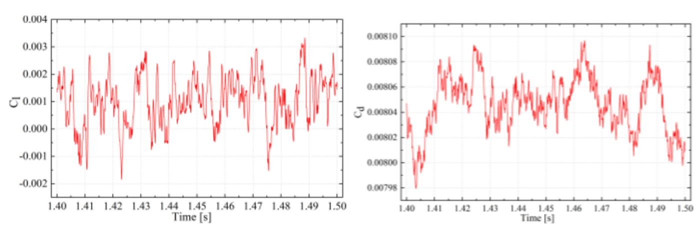

Fig. 4 Time history of C_l (left)and C_d (right) at AOA=0°

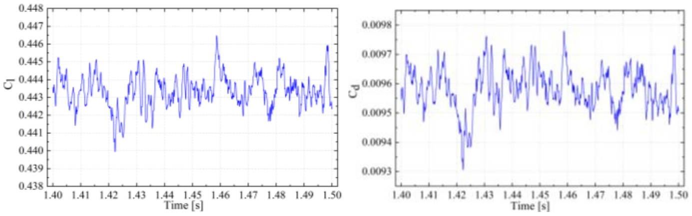

Fig. 5 Time history of C_l (left)and C_d (right) at AOA=4°

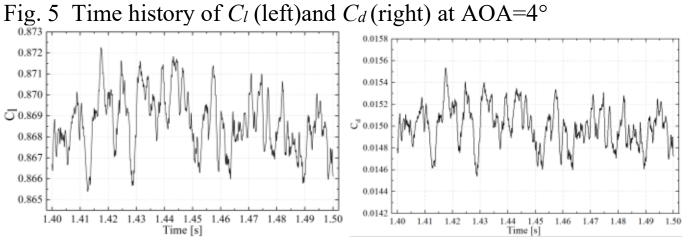

Fig. 6 Time history of C_l (left)and C_d (right) at AOA=8°

RESULT ANALYSIS

Flow Field Analysis

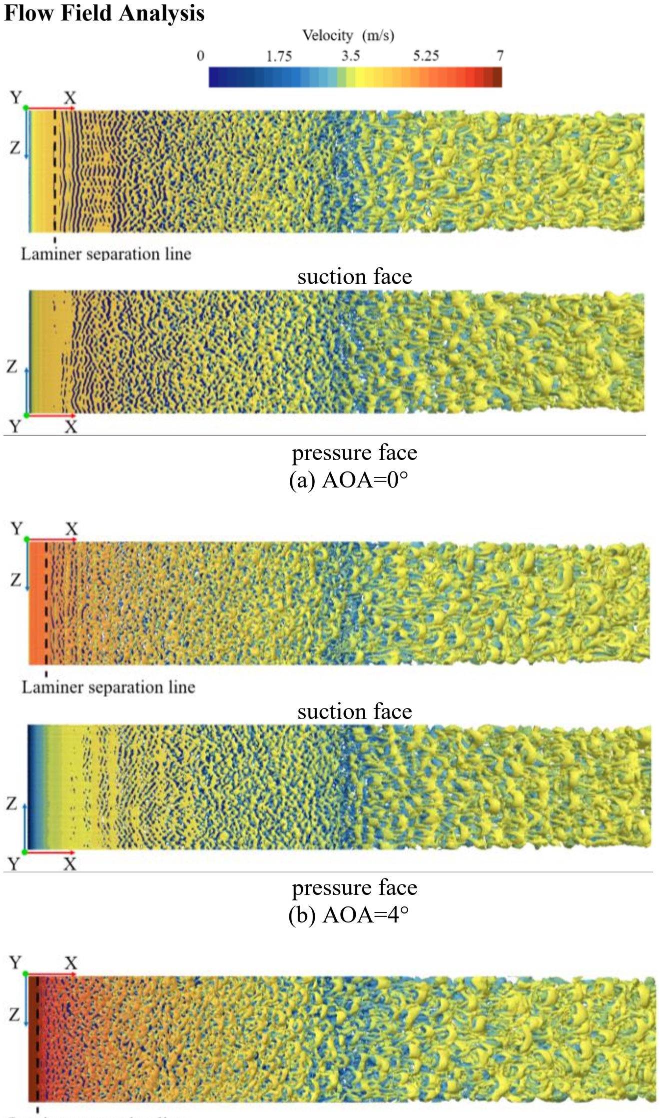

suction face

pressure face

(a) AOA=0°

suction face

pressure face

(b) AOA=4°

suction face

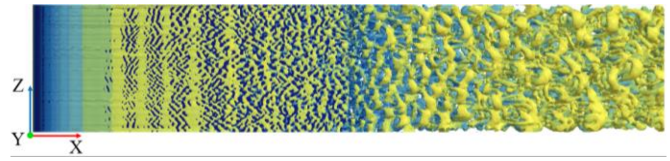

pressure face

(c) AOA=8°

Fig. 7 Instantaneous vortex structures, Q=2000 s^{-2}

The vortex structures at different AOA are illustrated in Fig. 7. At the current Reynolds number, no pronounced vortex shedding is observed. As the AOA increases, the laminar separation line on the suction side gradually shifts toward the leading edge, a trend that is consistent with the experimental observations reported by Seyhan M. *et al.* (2024). Once the turbulence becomes fully developed, the wake vortex structure is dominated by a horseshoe-shaped vortex pattern.

The distribution of turbulent kinetic energy on the mid-span longitudinal slice is shown in Fig. 8. As the AOA increases, regions of elevated turbulent kinetic energy near the leading edge (highlighted by the red area at the airfoil nose) become increasingly pronounced. This behavior is likely attributable to the more rapid pressure drop on the suction-side leading edge at higher angles of attack, which causes the flow to enter a region of strong adverse pressure gradient over a shorter arc length. When the momentum of the laminar boundary layer is insufficient to overcome this adverse pressure gradient, flow separation occurs earlier, resulting in enhanced turbulent kinetic energy.

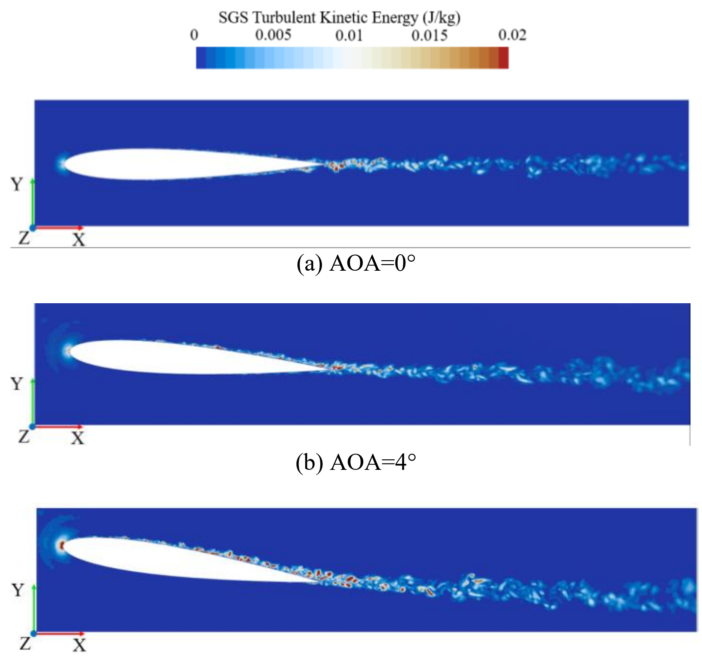

(a) AOA=0°

(b) AOA=4°

(c) AOA=8°

Fig. 8 Turbulent Kinetic Energy distribution

Acoustics Source Analysis

Following the approach proposed by Yu *et al.* (2025), the time derivative of pressure $\frac{d(pressure)}{dt}$ was employed as an approximate indicator of the dipole acoustic source term, The distributions on the suction surface at different AOA are presented in Fig. 9. When the flow has not fully developed into turbulence (i.e., within the transition region bounded by the two black dashed lines in the figure), the dipole source distributions at different angles of attack exhibit a pronounced stripe-like pattern with relatively regular and coherent structures. Once the flow becomes fully turbulent, the distributions become increasingly disordered.

As the AOA increases, the streamwise extent of the transition region gradually decreases, and the onset line (the first black dashed line on the left) moves closer to the leading edge. This behavior is closely related to the underlying flow dynamics, as higher AOA promotes earlier flow separation. The results further indicate that flow separation, through its influence on the temporal pressure fluctuations, plays a dominant role in the generation of dipole acoustic sources.

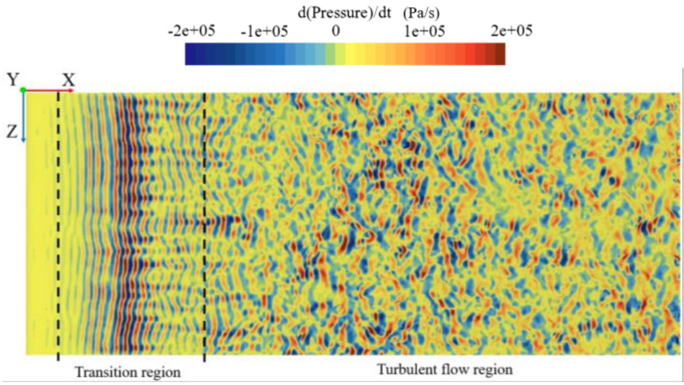

(a) AOA=0

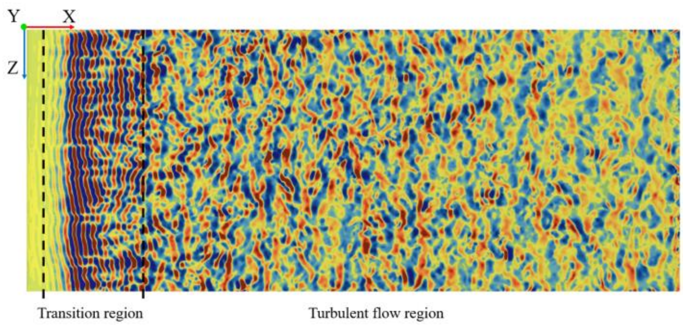

(b) AOA=4°

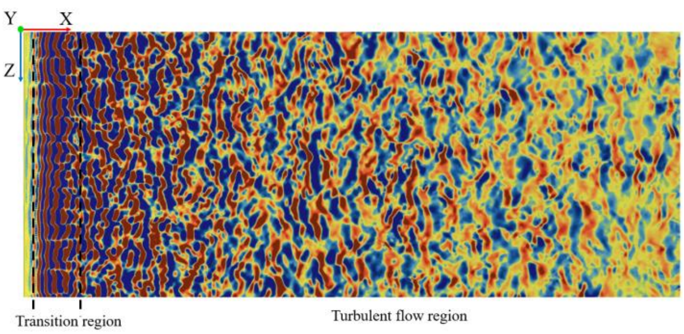

(c) AOA=8°

Fig. 9 Distribution of dipole source on the suction surface

Overall, the intensity of dipole source on the pressure side decreases with increasing AOA, as illustrated in Fig. 10. Specifically, the laminar region extends further downstream as the AOA increases, which is represented by the yellow region that extends from the leading edge downstream in the figure.

In conjunction with Fig. 11, it is observed that, when a nonzero angle of attack is present, the thickness of the dipole source region on the suction side face is greater than that on the pressure side at the same chordwise location. Additionally, distinct dipole characteristics are evident, as the red and blue regions, resembling small "protrusions," alternate in appearance. This also indicates that, in addition to the streamwise distribution, there is also a noticeable dipole source in the lateral direction, which is perpendicular to the flow direction. In the wake region, although no pronounced vortex shedding is observed, the evolution of flow structures still contributes significantly to the dipole acoustic source.

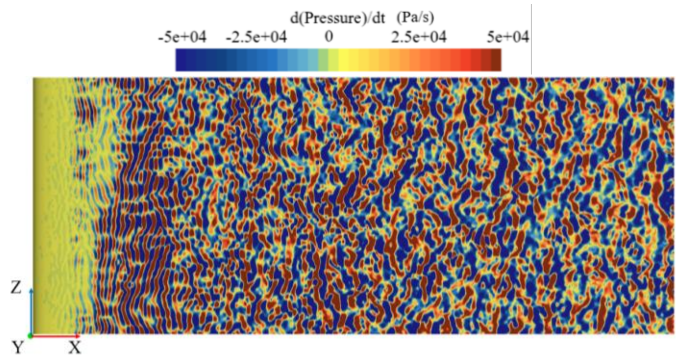

(a) AOA=0°

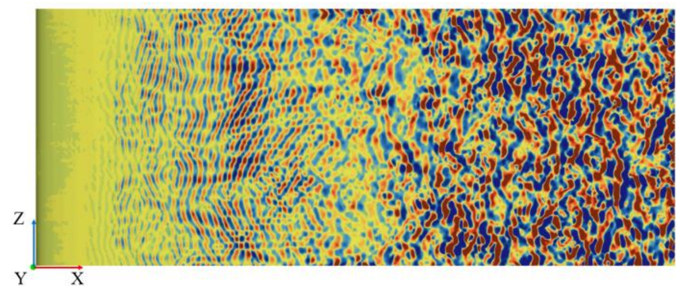

(b) AOA=4°

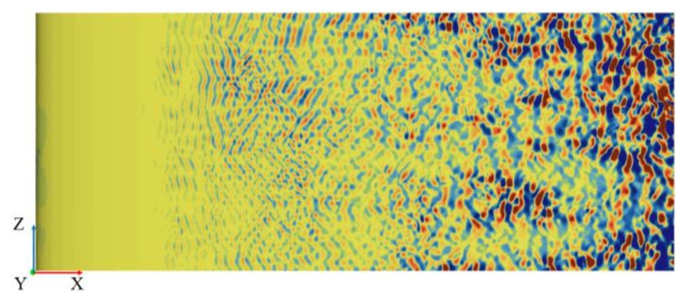

(c) AOA=8°

Fig. 10 Distribution of dipole source on the pressure surface

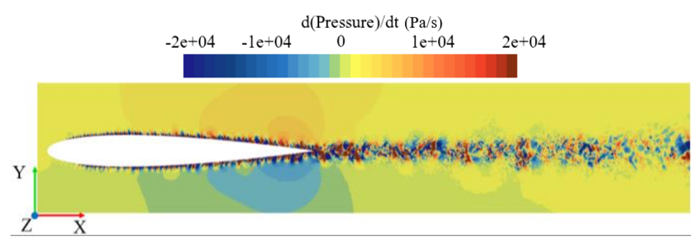

(a) AOA=0°

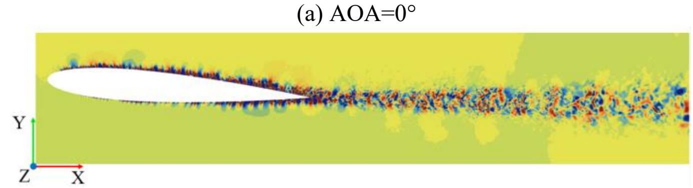

(b) AOA=4°

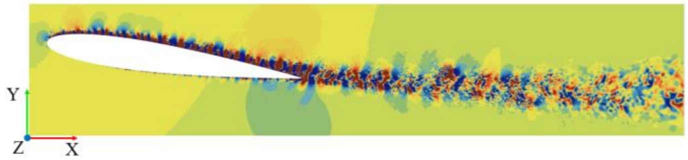

(c) AOA=8°

Fig. 11 Distribution of dipole source on the mid-span slice

The quadrupole acoustic source is represented by the second-order spatial divergence of the Lighthill stress tensor, $\frac{\partial^2}{\partial x_i \partial x_j}(T_{ij})$. The distributions on the suction and pressure surfaces are shown in Fig. 12, Fig. 13 , respectively.

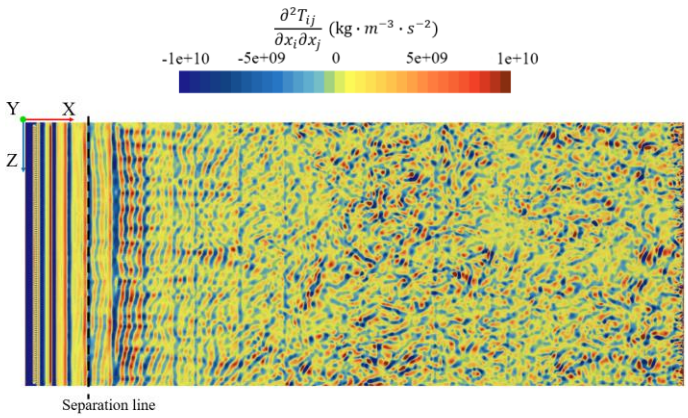

(a) AOA=0°

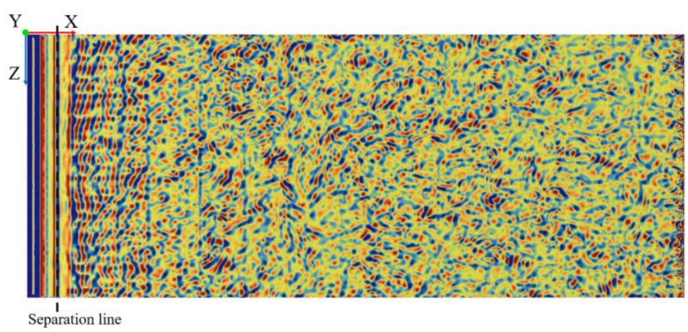

(b) AOA=4°

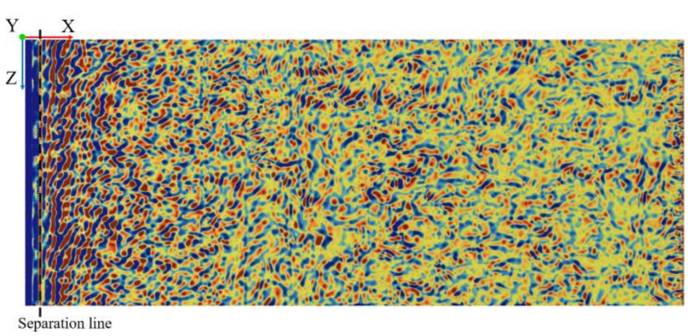

(c) AOA=8°

Fig. 12 Distribution of quadrupole source on the suction surface

Pronounced stripe-like patterns are also observed for the quadrupole sources near the leading edge. However, in contrast to the dipole sources, the stripe patterns of the quadrupole sources are nearly linear, whereas those of the dipole sources exhibit a curved structure. This difference may be attributed to the dominance of the $u_i u_j$ term in the Lighthill stress tensor at the present Reynolds number. In the vicinity of the leading edge, the flow remains predominantly laminar, and the streamwise velocity variation is relatively small. As a result, the quadrupole source distribution appears more regular, resembling straight-line patterns. As the AOA increases, the boundary separating the regular and irregular stripe patterns on the suction surface gradually moves toward the leading edge, as indicated by the black dashed lines in the figure. This behavior is qualitatively similar to that observed for the dipole acoustic source distributions, indicating that boundary-layer separation also has a discernible influence on the quadrupole acoustic sources.

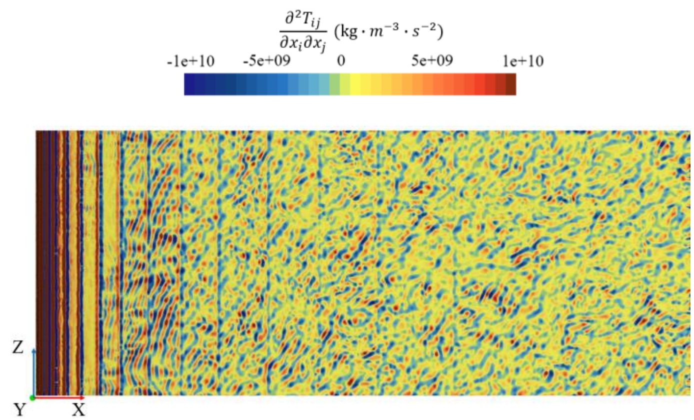

(a) AOA=0°

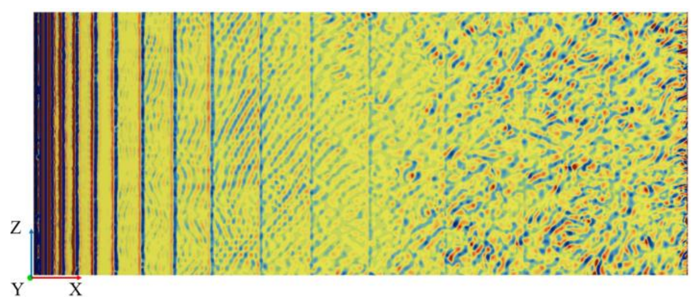

(b) AOA=4°

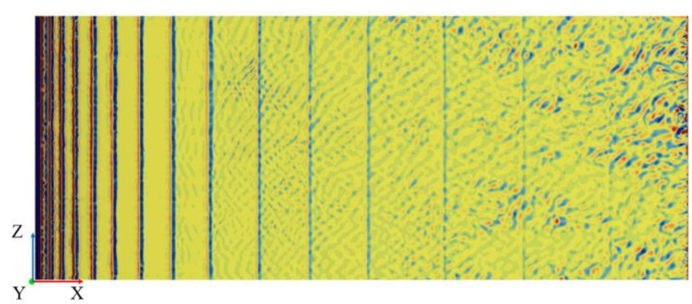

(c) AOA=8°

Fig. 13 Distribution of quadrupole source on the pressure surface

A slice of the mid-span longitudinal section is shown in Fig. 14. Compared with the dipole source distribution, the most prominent difference is the presence of four distinct alternating high- and low-intensity lobes near the leading edge. A similar phenomenon was also reported in the study by Hu Y. *et al.* (2022). This feature exhibits a clear quadrupole signature, thereby validating that the use of the second-

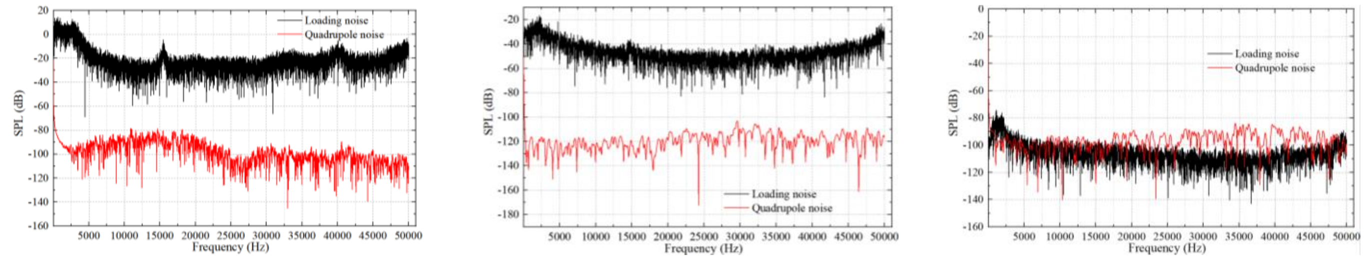

P1 P2 P3

(a) AOA=0°

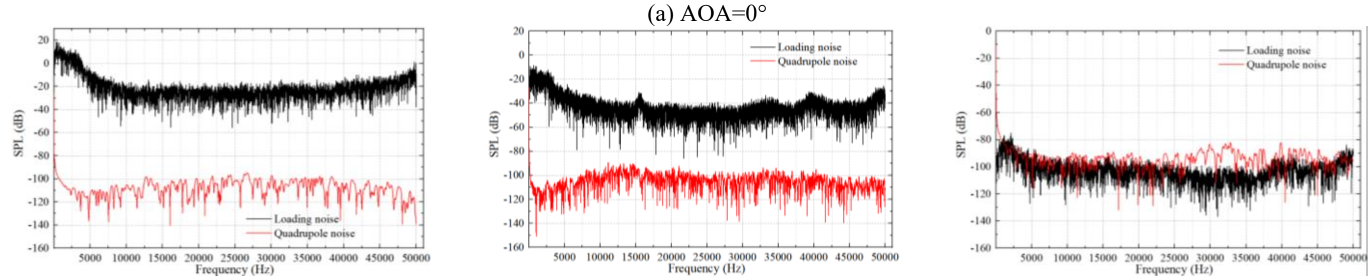

P1 P2 P3

(b) AOA=4°

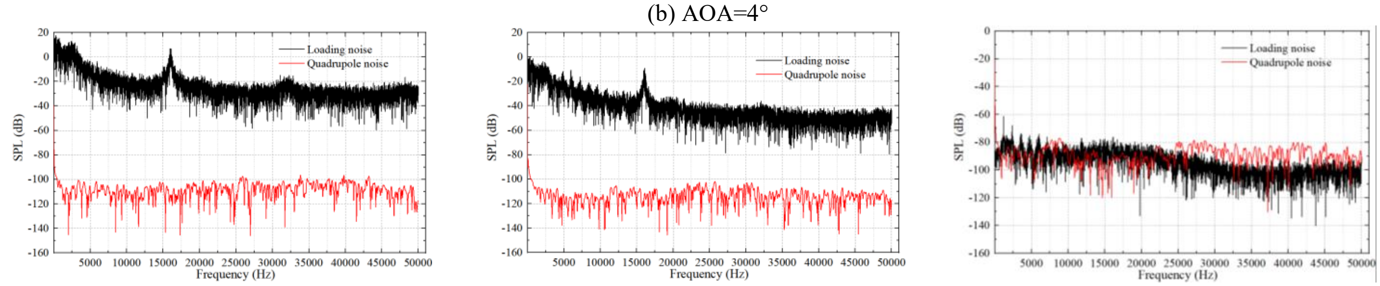

P1 P2 P3

(C) AOA=8°

Fig.15 Frequency spectrum analysis of noise at monitoring points

order spatial divergence of the Lighthill stress tensor $\frac{\partial^2}{\partial x_i \partial x_j}(T_{ij})$ as the acoustic source term is capable of capturing quadrupole characteristics. In addition, as the AOA increases, the quadrupole features near the leading edge on the suction side become increasingly pronounced along the streamline direction. This trend is manifested by an enlargement of the affected region, as highlighted by the black dashed boxes in the figure.

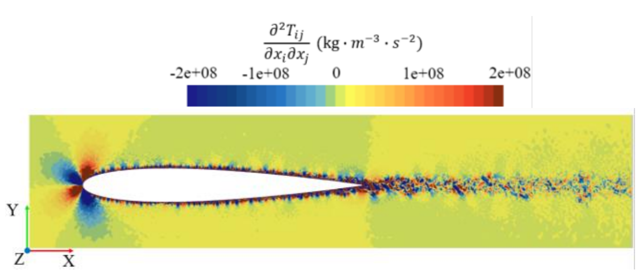

(a) AOA=0°

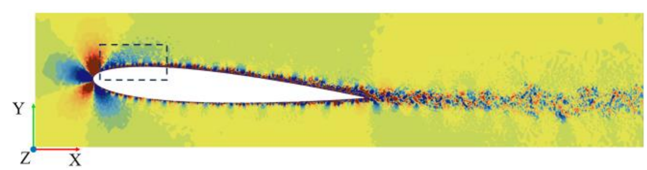

(b) AOA=4

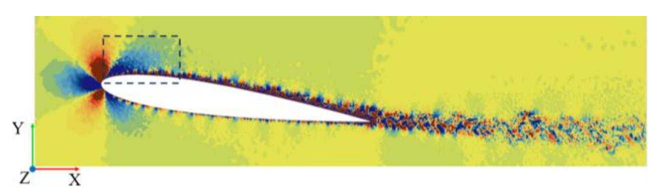

(c) AOA=8°

Fig. 14 Distribution of quadrupole source on the mid-span slice

Hydrodynamic Noise Analysis

The spectral analysis at different monitoring points is shown in Fig.15. At the same frequency, the SPL values of the dipole source at P1 and P2 are higher than those of the quadrupole source. Although the OASPL values of the quadrupole source at P3 is higher than that of the dipole source, this is primarily due to the contribution of high-frequency components above 25,000 Hz.

Table 4. Component analysis of the OASPL

	P 1 (dB)		P 2 (dB)		P 3 (dB)	
AOA	L	Q	L	Q	L	Q
0°	32.01	-27.51	-1.78	-38.76	-61.02	-14.3
4°	32.25	-27.31	8.76	-36.16	-60.16	-14.04
8°	32.3	-25.83	15.33	-31.6	-52.08	-8.49

Some scholars (J et al., 2018; M et al., 2018) argue that the quadrupole term is negligible for very low Mach numbers, while others (Cianferra et al., 2018, 2019) suggest that the impact of quadrupole noise may be greater than that of monopole and dipole noise. Therefore, this study conducts a quantitative analysis of the OASPL for dipole and quadrupole source to assess the influence of the quadrupole source. The OASPL values at the three monitoring points are shown in Table 4, where 'L' represents the loading noise and 'Q' represents the quadrupole noise.

Overall, at the same monitoring point, as the AOA gradually increases, both dipole and quadrupole noise OASPL values tend to increase. However, the specific data at different monitoring points vary. At point P3, for the same AOA, the OASPL of the dipole source is approximately 44 dB lower than that of the quadrupole source.

This may be because formula (7) contains a cos θ term, where θ is the angle between the normal vector ($\vec{n}$) at a point on the object's surface and the line connecting that point to the monitoring point (Fig.16). For point P3, many of these angles are close to 90°, resulting in a very small cos θ value, which in turn makes the OASPL of the dipole source very low. However, the surface source distributions in Fig. 9, Fig. 10, and Fig. 11, do not affect this outcome, as they are not linked to the monitoring points but are merely the surface distributions of the object itself.

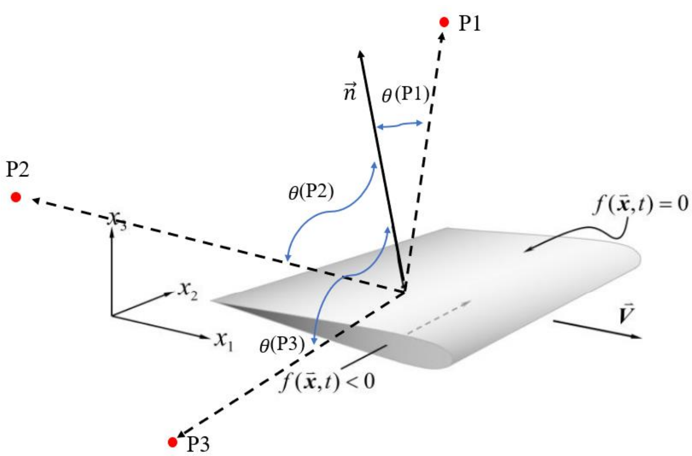

Fig.16 Schematic illustration of the θ for different monitoring points

Following this rationale, it is reasonable that the OASPL values at the P1 monitoring point remain consistently around 32 dB, with minimal sensitivity to changes in AOA. This can be attributed to the fact that, for P1, the cos θ value between the monitoring point and the surface points of the object is relatively larger, and the variation in AOA has a smaller effect on cos θ. In contrast, at the P2 point, the dipole noise is more strongly influenced by changes in AOA, with each variation exceeding 7 dB.

CONCLUSIONS

This paper takes the three-dimensional NACA 0012 as an example, at a Reynolds number of 360,000. The distributions of dipole and quadrupole acoustic sources were investigated under three different AOA 0°, 4°, 8°. The WALE model was employed for turbulence modeling. For acoustic prediction, the Farassat 1 A formulation of the FW-H acoustic analogy was adopted. All numerical simulations were conducted using the commercial software STAR-CCM+ (version 2302).

1. Flow field analysis reveals that as AOA increases, the laminar separation line on the suction surface of the hydrofoil gradually shifts towards the leading edge, while the laminar region on the pressure side extends downstream as the flow progresses.

2. As AOA increases, the OASPL values of both dipole and quadrupole acoustic sources at monitoring points in different azimuths exhibit a clear increasing trend. However, at the monitoring point located on the lateral side of the airfoil, the OASPL values of the quadrupole source exceed those of the dipole source. This is likely related to the position-dependent cos θ term in the Farassat 1A formula.

3. The spatial distribution of the acoustic sources is closely related to the flow structures. With increasing AOA, the irregular boundary of the dipole source distribution shifts upstream toward the leading edge, which is consistent with the behavior of boundary-layer separation in the flow field. The quadrupole-source identification method proposed in this study is able to distinctly capture quadrupole characteristics in the vicinity of the leading edge, and the resulting surface distribution exhibits a clear striped pattern.

In future work, Dynamic Mode Decomposition (DMD) could be employed to analyze acoustic source modes, studying the energy distribution of dipole and quadrupole sources at different frequencies on the surface of the underwater object, thereby providing further insight into flow-induced noise control technology.

REFERENCES

Bulut S, Ergin S (2023). “An investigation on hydro-acoustic characteristics of submerged bodies with different geometric parameters,” *Continuum Mechanics and Thermodynamics*, 35(3): 1123-1146.

Chen W, Qiao W, Tong F (2018).” Numerical investigation of wavy leading edges on rod–airfoil interaction noise,” *AIAA Journal*, 56(7): 2553-2567.

Cianferra M, Armenio V, Ianniello S (2018). Hydroacoustic noise from different geometries, *International Journal of Heat and Fluid Flow*, 70: 348-362.

Cianferra M, Ianniello S, Armenio V (2019). “Assessment of methodologies for the solution of the Ffowcs Williams and Hawkings equation using LES of incompressible single-phase flow around a finite-size square cylinder”, *Journal of Sound and Vibration*, 453: 1-24.

Deng F, Wang P, Yuan J (2025).” Turbulence model comparison for ventilated cavitation around a hydrofoil,” *Physics of Fluids*, 37(2).

Farassat, F (2007).” Derivation of Formulations 1 and 1A of Farassat”, *Technical Report NASA/TM-2007-214853*, NASA, Langley Research Center, Hampton, Virginia, USA.

Gregory N, O'reilly C L (1970). “Low-speed aerodynamic characteristics of NACA 0012 aerofoil section, including the effects of upper-surface roughness simulating hoar frost,” *London: Her Majesty's Stationery Office*.

Hu Y S, Wan Z H, Ye C C (2022). “Noise reduction mechanisms for insert-type serrations of the NACA-0012 airfoil”, *Journal of Fluid Mechanics*, 941: A57.

J. Keller, P. Kumar, and K. Mahesh (2018). “Examination of propeller sound production using large eddy simulation,” *Phys. Rev. Fluids* 3(6),

064601
Kim J W, Haeri S, Joseph P F (2016).” On the reduction of aerofoil–turbulence interaction noise associated with wavy leading edges,” *Journal of Fluid Mechanics,* 792: 526-552.
Li F, Huang Q, Pan G (2021). “Effect of hydrofoil leading edge waviness on hydrodynamic performance and flow noise”, *Ocean Engineering*, 231: 108883.
Ma Z, Li P, Wang L (2024). “Mechanistic study of noise source and propagation characteristics of flow noise of a submarine”, *Ocean Engineering*, 302: 117667.
M. Wang, S. K. Lele, and P. Moin (1996). “Computation of quadrupole noise using acoustic analogy,” *AIAA Journal*, 34(11), 2247–2254.
Nia B B, Ja'fari M, Ranjbar A R (2023). “Passive control of boundary layer flow separation on a wind turbine airfoil using vortex generators and slot”, *Ocean Engineering*, 283: 115170.
Ohman M D, Davis R E, Sherman J T (2019). “Zooglider: An autonomous vehicle for optical and acoustic sensing of zooplankton”, *Limnology Oceanography Methods*, 17: 69-86.
Seyhan M, Akbıyık H (2024). “An experimental investigation on the flow control of the partially stepped NACA 0012 airfoil at low Reynolds numbers”, *Ocean Engineering*, 306: 118068.
Sheldahl R E, Klimas P C (,1981). “Aerodynamic characteristics of seven symmetrical airfoil sections through 180-degree angle of attack for use in aerodynamic analysis of vertical axis wind turbines”, Sandia National Lab. (SNL-NM), *Albuquerque*, NM.
Simanto R I A, Hong J W, Pham V D (2025). “Effects of leading-edge protuberances on cavitation, induced noise and hydrodynamic performances of three-dimensional hydrofoils”, *Journal of Fluid Mechanics*, 1016: A56.
Xie B, Han H, Zhuang Y (2025). “Flow noise induced by an underwater vehicle with appendages”, *Physics of Fluids*, 37(8).
Xie B, Zhu J, Zhuang Y (2025). “Numerical Study of Flow Noise of an Underwater Vehicle with Different Attack Angles”, *International Ocean and Polar Engineering Conference*. ISOPE-I-25-254.
Yu L, Wan D, Shen Q, et al. Numerical study of flow-sound correlation mechanism and sound source distribution for NACA 0012 hydrofoil[J]. *Ocean Engineering,* 2025, 338: 122039.
Zhang, J., Huang, Z (2023). “Transient flow and noise characteristics of accelerated flow past a hydrofoil with special emphasis on vortex-turbulence-noise interaction”, *Ocean Engineering*. 268, 113427.